NUCL SCI TECH (2021) 32:91
https://doi.org/10.1007/s41365-021-00924-9

A compact electron storage ring for lithographical applications

Si-Qi Shen[1,2] · Da-Zhang Huang[3] · Zhen-Tang Zhao[1,2,3] · Qing-Lei Zhang[3]

Received: 14 April 2021 / Revised: 22 June 2021 / Accepted: 24 June 2021 / Published online: 3 September 2021

Abstract The physical design for a novel low-energy compact-storage-ring-based extreme ultraviolet (EUV) light source was systemically studied. The design process considers the linear and nonlinear beam optics, including transverse matching and the optimization of the dynamic aperture, momentum aperture, and beam lifetime. With a total circumference of 36.7 m and a beam energy of 400 MeV, the storage ring can operate with an average beam current of up to 1 A. With the undulator as the radiator, this facility has the potential to emit EUV radiation at 13.5 nm with an average power exceeding 10 W within the bandwidth. In addition, the collective instabilities of the lattice at high beam current were analyzed; it was found that the typical instabilities which may occur in an electron storage ring can be reasonably controlled in our design. With the advantages of variable beam energy and current, this design exhibits great promise as a new candidate for various EUV lithographical applications requiring tunable radiation power.

Keywords Storage ring · Extreme ultraviolet (EUV) · EUV lithography (EUVL)

This work was supported by the National Key Research and Development Program of China (No. 2016YFA0401901) and the National Natural Science Foundation of China (No. 11675248).

✉ Da-Zhang Huang
huangdazhang@zjlab.org.cn

[1] Shanghai Institute of Applied Physics, Chinese Academy of Sciences, Shanghai 201800, China

[2] University of Chinese Academy of Sciences, Beijing 100049, China

[3] Shanghai Advanced Research Institute, Chinese Academy of Sciences, Shanghai 201204, China

1 Introduction

With the recent rapid development of the microelectronics industry, the need for extreme ultraviolet lithography (EUVL) metrology has increased rapidly. Among many challenging tasks in EUVL metrology such as measuring the reflectivity of EUV multilayer coatings, characterizing the figure and finish of EUV mirror surfaces with high accuracy, and inspecting EUV mask blank substrates for pits and bumps and determining their flatness [1], the technical threshold of conventional EUV light sources such as laser-produced plasma sources is remarkably high [2], and these sources have several disadvantages as well. For example, to achieve higher levels of in-band EUV brightness, time-multiplexing of several sources is required, which increases both the cost and the complexity [3]. However, the recent development of electron-storage-ring-based light sources suggests a new approach to EUVL. New mechanisms such as stable-state microbunching and angular dispersion modulation have been studied [4–6], and machines have been designed and built, for example, the compact storage ring for actinic mask inspection (COSAMI) [7] and the Metrology Light Source [8].

However, because the EUV light sources for lithography are ultimately intended for use in industrial mass production, the performance-to-cost ratio is an essential consideration. For example, because the electron beam emittance is not highly important for photolithography, it can be less important in our design. Consequently, the lattice complexity and the cost can be dramatically decreased compared with those of the schemes mentioned above. Moreover, a higher emittance enables a higher bunch charge, which supports a higher radiation power. Therefore, a design study of a compact storage ring lattice with reduced complexity and relatively low cost for EUVL applications has been initiated.

In this study, our main goal was to systemically study the feasibility of a storage ring that can operate stably with an average beam current of up to 1 A and deliver EUV radiation with an average power suitable for lithographical applications such as wafer mask inspection. In addition, as mentioned above, to reduce the complexity of the machine and control the overall cost, little effort was made to decrease the emittance as long as the emittance is acceptable for the ring. The storage ring was optimized to obtain sufficient dynamic aperture for injection and ample momentum aperture to ensure the required beam lifetime. The working points were also analyzed to avoid the resonance lines as far as possible, and the bunch length was increased using the third harmonic cavity to increase the beam lifetime.

The remainder of this paper is organized as follows. In Sect. 2, we describe the lattice design, including the design and optimization of the linear and nonlinear beam optics. The lattice layout is presented, and the optimization of the dynamic and momentum apertures is discussed in detail. Frequency map analysis (FMA) and the evolution of the momentum aperture along the ring are also discussed. We estimate the beam lifetime when the third harmonic cavity is included. The injection scheme that will probably be used is also introduced. At the end of this section, the threshold of the typical collective instabilities is analyzed to estimate the stable operation of the machine, and more work is suggested to ensure good control of various collective effects. In Sect. 3, the undulator parameters are calculated to obtain the required EUV light, and the key indexes of the EUV light are also presented. The conditions for achieving it are analyzed, and concluding remarks are given in the last section.

2 Lattice design and optimization of the storage ring

2.1 Linear optics and dynamic aperture

The layout of the storage ring is illustrated schematically in Fig. 1. The racetrack-like lattice consists of four double-bend achromat cells, which minimize the lattice complexity and meet the basic requirements of the storage ring for acceptable beta functions and dispersion, and two long straight sections each 8 m in length. These sections are reserved for insertion devices such as the undulator,

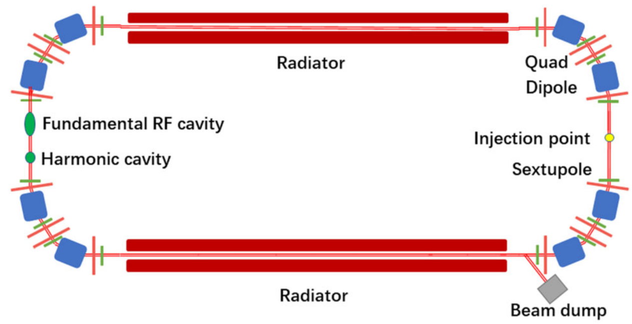

Fig. 1 (Color online) Schematic of racetrack-like storage ring light source. Blue, green, and red indicate bending magnets, quadrupole magnets, and sextupole magnets, respectively, and the radiators are shown in deep red

also called a radiator, which will generate radiation. The total circumference of the ring is 36.7 m, and it will operate at the 61st harmonic of the 500 MHz fundamental radio frequency (RF). A storage ring energy of 400 MeV is chosen to reduce the required RF power and to obtain the desired EUV wavelength. The natural emittance is approximately 44 nm·rad in the horizontal direction, and the average beam current is 1 A so that photons with the necessary flux and power can be produced. The basic parameters of the ring are shown in Table 1.

The integer of the fundamental RF wavelength was chosen as the total length of the ring. There are two bending magnets, four quadrupoles, and four sextupole magnets in each cell. The bending magnets are all 0.816 m in length and have a bending angle of 45°. The phase advance of the reference particle is adjusted by changing the strengths of the quadrupoles to optimize the working point, i.e., by horizontal and vertical tuning, to avoid various types of resonance such as external resonance, parametric resonance, and sum, and difference resonance [9]. The goal is to ensure the stability of the closed orbit of the particle and to obtain horizontal and vertical orbits that are closed to each other in the straight sections. After the linear optics were optimized, the main parameters of the storage ring were determined. The optimization was performed using the NSGA-II program. The typical optical functions of the lattice are shown in Fig. 2.

The sextupole magnets are used to correct the chromaticity and to optimize the dynamic and momentum apertures. There are four sextupoles in each cell. Two are used to obtain positive chromaticity; they are called the chromatic sextupoles and are located between the two bending magnets, where the dispersion is large. The other two sextupole magnets, which are called harmonic sextupoles, are employed to optimize the dynamic aperture, which should be large enough for injection, and to optimize the momentum aperture for a longer beam lifetime. These

Table 1 Basic parameters of storage ring

Element	Value
Total circumference including straight section (m)	36.7
Straight section (m)	2×8.0
Total length of dipoles (m)	8×0.816
Harmonic number	61
Energy (MeV)	400
Working points ($\nu_x/\nu_y/\nu_z$)	3.22/1.36/0.0118
Average beam current (A)	>1
Energy loss per turn (keV)	2.18
Horizontal natural emittance (nm rad)	43.8
Chromaticity (horizontal/vertical)	0.1231/0.048
Radiation damping time (horizontal/vertical/energy) (ms)	33.0/44.9/27.4
Bunch length w/o third harmonic cavity (mm, rms)	3.5
Bunch length w/third harmonic cavity (mm, rms)	14.2
RF voltage of the fundamental cavity (MV)	50
RF voltage of third harmonic cavity (MV)	16.7

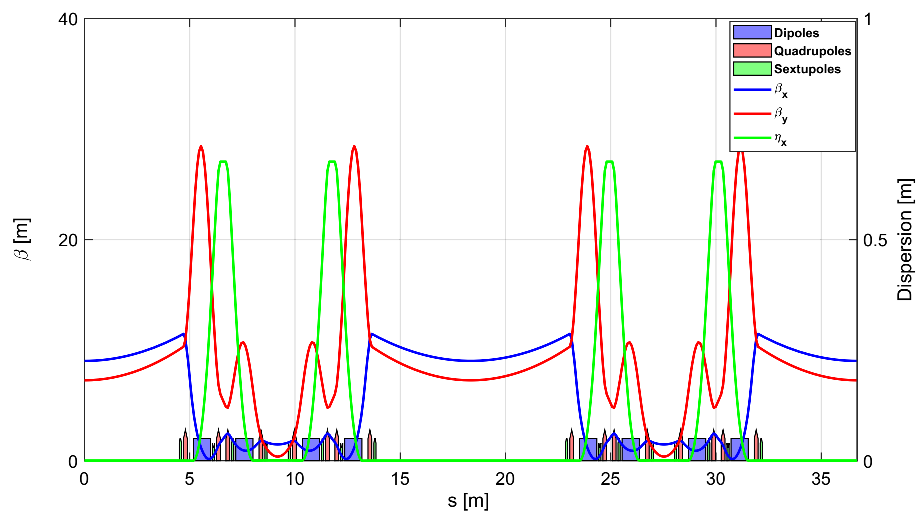

Fig. 2 (Color online) Typical optical functions of the lattice. The blue curve is the horizontal beta function, the red curve is the vertical beta function, and the green curve is the horizontal dispersion function

two magnets are placed at the ends of the bending magnets near the long straight section, where the dispersion is zero.

The chromaticity is defined as the derivative of the transverse tune over the relative momentum spread of a particle. It arises because the quadrupoles exert different focusing forces on particles of different energies. Therefore, there is always a natural chromaticity (Eq. 1) provided by the quadrupole magnets in the storage ring. The natural chromaticity is usually negative because the focusing force on higher-energy particles is weaker [9].

$$C_{x,y,\mathrm{nat}} = \frac{-1}{4\pi} \oint \beta_{x,y} K_{x,y} \mathrm{d}s, \tag{1}$$

where β is the beta function, K is the strength of the quadrupole, and x and y represent the horizontal and vertical directions, respectively. Negative chromaticity will cause the difference $\Delta\nu$ between particles with different energies to increase, and thus $\nu_{x,y}$ will be close to the resonance value. To avoid negative chromaticity, the chromatic sextupoles are placed at locations where the dispersion is large, and the chromaticity can be reduced to zero by using the higher-order focusing term of the sextupole magnets (Eq. 2) [9].

$$C_{x,y} = \frac{-1}{4\pi} \oint \beta_{x,y} \left[K_{x,y}(s) - S(s)D(s)\right] \mathrm{d}s, \tag{2}$$

where S represents the sextupole strength, and D is the dispersion. During optimization, it is difficult to obtain zero chromaticity in the horizontal and vertical directions simultaneously. Therefore, the chromaticity is usually optimized to positive values slightly larger than zero to ensure that particles with higher energy receive a stronger focusing force so that $\Delta\nu$ between particles is controllable.

The dynamic aperture of the beam in a storage ring is usually defined as the phase space area in which particles cannot be lost after multiple revolutions. The area of the transverse cross-section of the beam is usually employed to define the dynamic aperture. Because of the tune spread of the beam and the nonlinear focusing force, the particles falling on the resonance lines will be lost. This determines the maximum transverse area in which beam particles can survive, which is the dynamic aperture. Because the focusing force is nonlinear, sextupole families are used for optimization.

The chromaticity should remain constant during the maximization of the dynamic aperture. Thus, the harmonic sextupole magnets, used for optimization, are usually placed at locations where the dispersion is close to zero, and the dynamic aperture is optimized by adjusting the strengths of these magnets. For further optimization, octupole magnets could also be added in the future to eliminate higher-order terms.

In the optimization process, we used the beam tracking code Elegant [10], and we used its built-in simplex algorithm for multi-objective optimization. The goal was to optimize the driving terms related to the chromaticity, tune, and particle momentum of the bunch (first and second order) [11]. The optimized variables are the strengths of the harmonic sextupoles [12]. The convergence of the results indicates that the optimal condition was reached. Moreover, radiation damping and quantum excitation were also taken into account to obtain more realistic results.

Figure 3 shows the FMA diagram of the optimized storage ring. Colors represent the logarithm of the tune difference ($\Delta\nu$) between an arbitrary beam particle and the reference particle. The region, where $\Delta\nu$ is relatively uniform, is considered the dynamic aperture of the beam. The figure shows that the dynamic aperture of the beam reached several centimeters in diameter in the transverse direction after optimization, which meets the beam injection requirements of the storage ring. Figure 4 shows the working points, which were obtained by taking the beam energy spread into account. The data points in the figure represent the fractional tunes in both the horizontal and vertical directions. The resonance lines up to the fourth-order resonance are drawn. Most of the working points within the dynamic aperture (blue) are not on resonance lines.

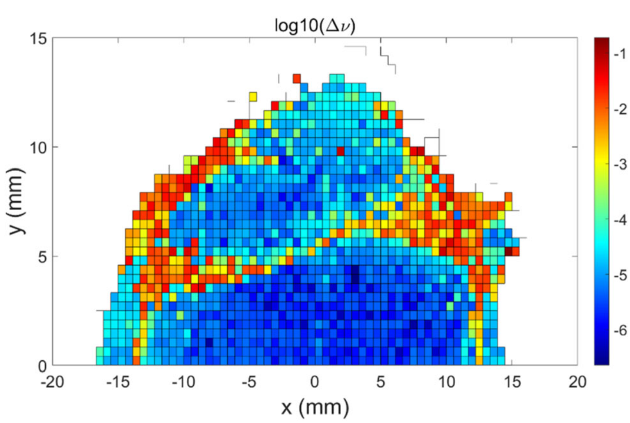

Fig. 3 (Color online) FMA diagram of the ring

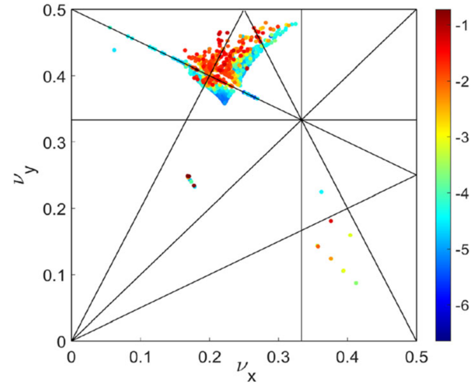

Fig. 4 (Color online) Working points of the ring considering the beam energy spread

Figure 5 shows the dynamic aperture, with error bars, before and after orbit correction. Each cell was divided into two parts on separate girders. The installation errors were set to 50 μm in both the horizontal and vertical directions within the girder and 80 μm between the girders, with 3 σ truncation. For orbit correction, four correctors and three beam position monitors (BPMs) were added to each cell, and all the correctors were combined with the sextupoles. Accelerator toolbox (AT) [13] was employed to track the beam for 5000 turns. The result shows that the average dynamic aperture of the beam can reach $\pm$ 10 mm in the horizontal direction and $\pm$ 7 mm in the vertical direction. In addition, the minimal dynamic aperture after orbit correction, considering the error bars, is approximately $\pm$ 7

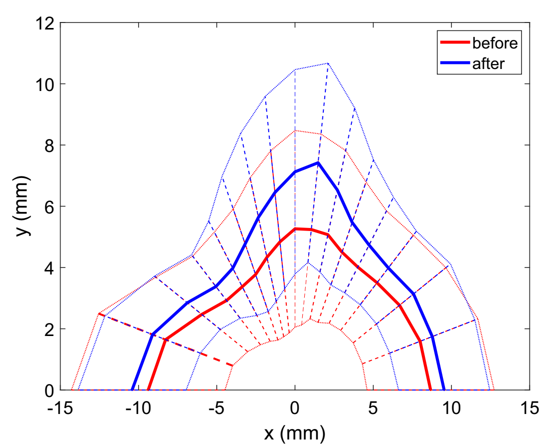

Fig. 5 (Color online) Dynamic aperture, with error bars, before (red) and after (blue) orbit correction

and $\pm$ 5 mm in the horizontal and vertical directions, respectively. Therefore, the dynamic aperture after orbit correction meets the injection requirements.

In the last part of this section, we briefly introduce the injection scheme that will probably be used for the main ring. First, a booster ring is needed to accumulate and inject the beam in top-up mode to achieve stable injection with a current variation of less than 0.1%. The booster will be placed immediately above or below the main storage ring to save space. In the scheme, the beam is extracted by a kicker magnet with a rapid rise time and immediately deflected toward the storage ring by a septum magnet [14, 15]. A slow orbit bump is employed to generate a displacement of < 10 mm horizontally at the septum position. A linac injector with a photocathode electron gun will also be installed near the booster ring to supply the electron beam.

2.2 Momentum aperture, higher harmonic cavity, and beam lifetime

In a low-emittance storage ring, the Touschek lifetime dominates the beam lifetime [16]. Touschek scattering causes the loss of electrons and determines the lifetime. Transverse scattering results in large energy kicks to particles, which undergo betatron oscillation and are lost rapidly on the physical aperture. The loss rate is proportional to the particle density in the bunch and inversely proportional to the momentum acceptance, which is also called the momentum aperture. The rate of beam loss due to the Touschek effect takes the form [17]

$$\frac{1}{T} = \frac{r_{\mathrm{e}}^2 c N_{\mathrm{e}}}{8\sqrt{\pi}\beta^2\gamma^4\sigma_z\sigma_{\mathrm{p}}\varepsilon_x\varepsilon_y}\langle\sigma_{\mathrm{H}}F(\delta_{\mathrm{m}})\rangle, \tag{3}$$

where T stands for the Touschek lifetime, and $\langle\ldots\rangle$ represents the average throughout the entire ring.

Similar to the dynamic aperture, the momentum aperture represents the momentum/energy tolerance of the beam. As above-mentioned, when the energy spread is too large, particle loss can occur. On the other hand, a larger momentum aperture corresponds to a longer Touschek lifetime, which means that the upper limit of the momentum aperture determines the Touschek lifetime. Touschek scattering is the large-angle scattering from the transverse to the longitudinal direction and excites the large-amplitude betatron oscillation of scattered particles, which will cause the beam to be lost if the oscillation exceeds the physical aperture of the machine, limiting the beam lifetime. The momentum aperture of the beam is the key factor that determines the Touschek lifetime. It can be estimated by numerical beam tracking. A positive momentum kick $[\delta_{\mathrm{m}}(s)]$ is given to a particle in the bunch at a given position (s), causing it to undergo betatron oscillation. The maximum kick that the particle can withstand without loss after numerous turns is the positive momentum aperture. The negative momentum aperture can be obtained by the same method using a negative kick.

We used Elegant to calculate and optimize the momentum aperture of the beam [18]. The optimization method and algorithm are the same as those used to compute the dynamic aperture. In the optimization process, radiation damping by both the bending magnets and undulators was included, along with the RF cavities. In addition, the physical aperture was taken as $\pm$ 2.5 cm horizontally and $\pm$ 4 mm vertically in the straight section considering the undulator gap. To ensure that the damping time is sufficiently long for the beam to reach the stable state, we calculated the momentum aperture after numerous turns. We found that when the beam was tracked for more than 10,000 turns, the result remained essentially unchanged, as shown in Fig. 6. We expect that additional work will further maximize the momentum aperture.

According to Eq. (3), the Touschek lifetime is determined by the number of particles in the bunch, beam energy, beta function, transverse emittance, and bunch length. Among these parameters, the transverse emittance and bunch length are most often tweaked to optimize the lifetime. The former can be adjusted by changing the horizontal/vertical coupling ratio, and the latter can be increased by inserting a higher-order harmonic cavity into the lattice.

A cavity with a resonant frequency that matches the harmonics of the fundamental RF in a storage ring is called a higher-order harmonic cavity. Its main function is to adjust the beam energy to control the beam dynamics by adjusting either the energy of electrons at different locations in the beam or that of different bunches in the bunch train. The higher-order harmonic cavity interacts with the beam in different ways to stretch or compress the bunch, and the harmonics of the cavity determine the cavity size [19]. In the storage ring, we designed the fundamental RF

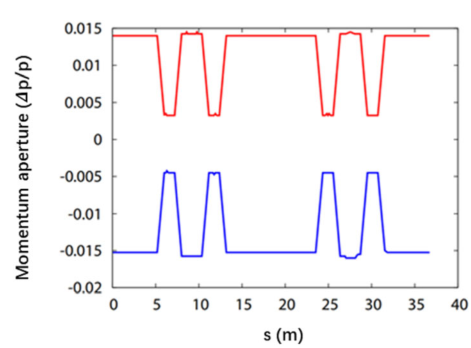

Fig. 6 (Color online) Variation of the momentum aperture throughout the lattice after 10,000 turns

in the ring is approximately 500 MHz, and we chose a frequency of 1.5 GHz for the high-order harmonic cavity; thus, the harmonic number is 3.

The bunch length in the time domain can be calculated as

$$\sigma_{hl} = \frac{2\sqrt{\pi}}{\Gamma\left(\frac{1}{4}\right)}\left(\frac{3}{n^2-1}\right)^{\frac{1}{4}}\left(\frac{\alpha_c\omega_{RF}\sigma_E}{\omega_s E_0}\right)^{\frac{1}{2}}\frac{c}{\omega_{RF}}, \tag{4}$$

where n is the harmonic number, α_c is the momentum compaction factor,ω_{RF} is the frequency of the fundamental RF cavity, σ_E is the energy spread, ω_s is the angular frequency of synchrotron oscillation without the harmonic cavity, E_0 is the energy of the storage ring, c is the speed of light, and $\Gamma\left(\frac{1}{4}\right) = 3.6256$.

To illustrate the problem, we substitute the cavity voltage into the longitudinal motion equation of the beam to obtain the potential well as a function of RF phase when the harmonic cavity is present:

$$\begin{aligned} U_w(\phi) &= \cos\phi - \cos\phi_s + \frac{k}{n}\{\cos[n(\phi-\phi_s)+\phi_n]\} \\ &\quad + (\phi-\phi_s)\cdot\sin\phi_s + k\cdot\sin\phi_n. \end{aligned} \tag{5}$$

For comparison, the potential well without the harmonic cavity reads

$$U_{wo}(\phi) = (\phi-\phi_s)\cdot\sin\phi_s - \cos\phi_s + \cos\phi, \tag{6}$$

where ϕ is the RF phase, and ϕ_s is the synchrotron phase. By comparing Eqs. (5) and (6), we can see that the potential well is lengthened, which provides more space to hold a longer bunch, as shown in Fig. 7.

Therefore, to obtain a sufficient Touschek lifetime for a high beam current, we introduce a third harmonic cavity into the lattice to increase the bunch length from 3.5 to 14.2 mm rms. Considering the natural coupling in the ring introduced by misalignments, magnet tilts, dispersion leaks, etc., we take the coupling value to be 10%. From Fig. 4, we can see that the minimum momentum aperture ($-0.5\% - 0.3\%$) appears at the locations of the dipoles, and the maximum aperture ($\sim \pm 1.5\%$) almost fills the rest of the lattice, which is more than 80% of the total length. As a result, using Elegant calculations, we obtained average Touschek lifetimes of approximately 1.3 h at an average beam current of 1 A weighted over the length of regions with different momentum apertures with a 10% vertical/horizontal coupling ratio and of approximately 40 min at 2 A. These values are acceptable for this high beam current in top-up mode. Note that all the RF buckets will be filled with electrons; thus, the charge of a single bunch at 1 A is 2 nC at a fundamental RF of 500 MHz. The possibility of ion instability is discussed in Sect. 2.3.

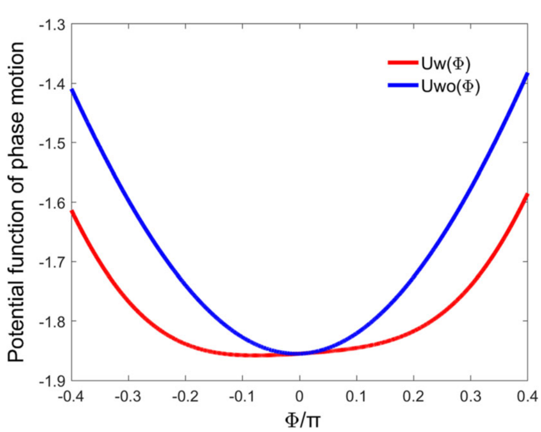

Fig. 7 (Color online) Potential well with (red) and without (blue) the third harmonic cavity. Note that the horizontal axis has units of the ratio of the RF phase over π

2.3 Estimation of collective effects

In this subsection, we roughly estimate the possible collective effects in our ring to ensure that the machine can operate stably. As noted above, the design goal is an average beam current of up to 1 A, which is quite high. Thus, the collective effects could play an important role in our machine.

The sources of collective effects may include electron clouds, ions, and impedance elements in the ring. The impedance elements in the ring cause various instabilities, which often limit high-current operation, and interactions between an electron cloud and ions usually introduce beam-ion instabilities, including ion traps and fast ion instability (FII) at high beam currents. In this section, we discuss the typical instabilities that may appear in our ring.

When a charged particle moves in a beam pipe, it will excite an electromagnetic field if the shape of the pipe changes or resistance is present in the pipe wall. Because this field is behind the source particle, it is called the wakefield. In many cases, the wakefield takes some time to decay; therefore, it affects the trailing particles and may introduce instabilities [20]. In a real machine, we would observe the spectra of the beam. In addition, because the beam dynamics is usually analyzed in the frequency domain, we performed a Fourier transform of the wakefield to obtain the impedance, for example, s.

$$Z(\omega) = \frac{1}{c}\int_{-\infty}^{+\infty} w(s)e^{\frac{i\omega s}{c}}\mathrm{d}s, \tag{7}$$

where s is the longitudinal coordinates of the witness particle.

The narrowband impedance usually results in coupled-bunch instability. The introduction of broadband impedance generally excites microwave instability in both the transverse and longitudinal directions. In the following, we outline both the narrowband and broadband impedance and their effects on the collective instabilities in our ring.

The resistive-wall (RW) impedance can be both narrowband and broadband [16]. In addition, because the resistive beam pipe occupies most of the length of the ring, the RW impedance plays a major role in our design. As an example, we estimated the longitudinal coupled-bunch instability by comparing the impedance threshold, as shown in Eq. (8).

$$Z_{\mathrm{th}}^{\parallel} = \frac{4\pi Q_{\mathrm{s}}\left(\frac{E_0}{e}\right)}{I_0\omega\eta\tau_{\mathrm{S}}}, \tag{8}$$

where E_0 is the beam energy, τ_{S} is the longitudinal radiation damping time, I_0 is the average beam current, Q_{s} is the synchrotron tune, ω is the frequency of the wakefield, η is the momentum compaction factor, and the longitudinal RW impedance is given by Eq. (9) [21].

$$Z_{\parallel}^{\mathrm{RW}}(\omega)/n = \frac{\mu Z_0}{2\mu_0 b}\left(\frac{2\rho_{\mathrm{c}}}{\mu\omega}\right)^{1/2}, \tag{9}$$

where $Z_{\parallel}^{\mathrm{RW}}/n$ is the effective longitudinal impedance, $Z_0 \approx 377\Omega$ is the vacuum impedance, ρ_{c} is the material resistance, b is the pipe radius, μ is the material permeability, and μ_0 is the free space permeability. Figure 8 compares the effective longitudinal RW impedance and the threshold of the longitudinal coupled-bunch instability as a function of frequency, which was calculated using the parameters in Table 1 with a 1 A average beam current. Copper was selected as the material of the vacuum pipe, which has an inner radius of 25 mm and a wall thickness of 1.5 mm.

In Fig. 8, we can see that the effective longitudinal RW impedance is below the threshold up to 20 GHz, which covers almost all the possible bandwidth of the instability. However, the longitudinal narrowband geometric impedance introduced by the RF cavities, kickers, BPMs, etc., produces additional small peaks on the RW impedance curve in Fig. 7. Among them, the higher-order modes of the RF cavity can be the most harmful sources of coupled-bunch instability. Therefore, the cavities in our rings will be carefully designed. Nonetheless, although more work is necessary to investigate the details, on the basis of past experience and a comparison with the RW impedance given above, we are confident we can design and build devices that satisfy the threshold.

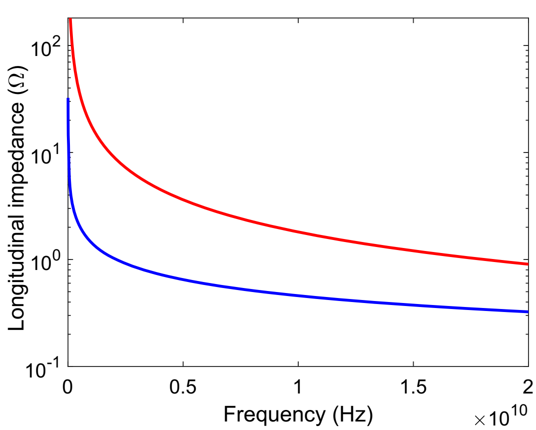

Fig. 8 (Color online) Comparison of impedance threshold of longitudinal coupled-bunch instability (red) and effective longitudinal RW impedance (blue)

Next, as is well known, the RW instability usually refers to the transverse coupled-bunch instability arising from the long-range RW wakefields. Therefore, we also estimated the transverse coupled-bunch instability by calculating the current threshold at zero chromaticity [16], which is the worst case of the instability, and it reads

$$I_{\mathrm{th,RW}} = \frac{4\pi E/eb^3}{c\beta_{\perp}\tau_{\perp}}\left[\frac{(1-\Delta Q_{\beta})\tau_{\perp}\omega_0}{2cZ_0\rho_{\mathrm{c}}}\right]^{\frac{1}{2}}, \tag{10}$$

where $\tau_{\perp}$ is the transverse radiation damping time, $\beta_{\perp}$ is the average of the beta function along the ring, and ω_0 is the angular revolution frequency of beam particles. ΔQ_{β} is the fractional part of the betatron tune, and the other variables are defined above. The result obtained using the beam parameters in Table 1 shows that the average current threshold is approximately 80 mA. Although the nominal design current of our machine is 1 A, which gives a ratio of 12 between the two currents, the instability is still within the range that a standard transverse feedback system can currently handle [13, 20].

The longitudinal broadband impedance can introduce longitudinal microwave instability. When this instability occurs, the longitudinal current distribution of the beam is impaired, and the energy spread increases. As a result, the beam quality deteriorates, and beam loss may occur. We estimated the impedance threshold of a single bunch for the longitudinal microwave instability in a storage ring on the basis of the Keil–Schnell criterion for a coasting beam [9, 22], which was extended to a bunched beam by Boussard [16].

$$\left|\frac{z}{n}\right|_{\mathrm{eff}} = \frac{\sqrt{2\pi}\eta\left(\frac{E_0}{e}\right)\sigma_{\mathrm{E0}}^2\sigma_{10}}{RI_{\mathrm{b}}}, \tag{11}$$

where R is the average radius of the storage ring, E_0 is the energy of the storage ring, σ_{E0} is the energy spread, σ_{l0} is the bunch length, η is the phase slip factor, I_{b} is the bunch current, and $|z/n|_{\mathrm{eff}}$ is the effective longitudinal impedance.

Our machine is designed for operation at an average beam current of 1 A with a harmonic number of 61. Thus, if we choose a single-bunch current of 16.4 mA, the total effective broadband impedance will be less than 0.39 Ω, according to Eq. (11). For comparison, the total effective broadband impedance of the SSRF is approximately 0.17 Ω, and those of Soleil and BEPC are approximately 0.21 and 0.23 Ω, respectively. Therefore, we believe that microwave instability will not be a problem in our machine.

In addition to the longitudinal microwave instability, the transverse broadband impedance may also introduce another single-bunch instability called the transverse mode coupling instability (TMCI) or the fast head-tail instability, which is also detrimental to the machine. TMCI occurs when the frequencies of two neighboring head-tail modes approach each other because of detuning with increasing current during accumulation [21]. To estimate the effect, we first compute the transverse broadband impedance from the longitudinal broadband impedance and the Panofsky–Wenzel theorem.

$$Z_{\perp}^{\mathrm{BB}} \approx \frac{2R}{b^2}\frac{Z_{\parallel}}{n} \tag{12}$$

Like that in the longitudinal direction, the single-bunch current threshold of the TMCI can be derived as [23]

$$I_{\mathrm{th}} = \frac{4\left(\frac{E_0}{e}\right)Q_{\mathrm{s}}}{Z_{\perp}^{\mathrm{BB}}\beta_{\perp}R}b, \tag{13}$$

where $\beta_{\perp}$ represents the average beta function over the machine. In our design, the radius of the beam pipe is 25 mm; thus, the single-bunch current threshold of the transverse microwave instability is 82.6 mA, which is much larger than the longitudinal single-bunch current threshold of our machine. Therefore, the transverse microwave instability and TMCI will not be a problem either. Finally, it is necessary to note that the chromaticity is conventionally adjusted to a positive value to avoid the TMCI, whereas positive chromaticity usually results in certain higher-order modes of another transverse instability called the head-tail instability, and the threshold of the first unstable mode of the instability is even lower than that of the TMCI [16]. The patterns of the instability are different at low and high positive chromaticity and have been studied at ESRF [24]. Thus, caution should be used in designing the chromaticity in our machine.

To achieve an average beam current of up to 1 A, all the RF buckets throughout the ring will be filled with electrons. Consequently, another collective effect called the ion instability, which includes ion trapping and the FII, had to be estimated because of the limited spacing between beam bunches. The instability arises from interactions between the electron beam and the ionized residual gas, and it induces transverse center-of-mass oscillation of the beam. The growth time of the ion trap instability is generally long, and it can be alleviated by introducing bucket gaps, which are usually approximately a few percent of the ring circumference, behind the bucket train during filling. However, in modern storage rings, the single-pass FII is more significant owing to the small emittance and multi-bunch operation. The asymptotic growth rate of the FII derived by Raubenheimer and Zimmermann for a flat beam is given by [25]

$$\tau_{\mathrm{asymp}}^{-1}[\mathrm{s}^{-1}] \approx \frac{N_{\mathrm{e}}^{\frac{3}{2}} n_{\mathrm{b}}^{2}}{\gamma}\left[5p_{\mathrm{gas}}[\mathrm{torr}]\frac{r_{\mathrm{e}} r_{\mathrm{p}}^{\frac{1}{2}} L_{\mathrm{sep}}^{\frac{1}{2}} c}{\sigma_y^{\frac{3}{2}}\left(\sigma_x+\sigma_y\right)^{\frac{3}{2}} A^{\frac{1}{2}}}\right], \tag{14}$$

where N_{e} denotes the number of electrons in a bunch, n_{b} is the number of bunches in the train, γ is the relativistic factor, p_{gas} is the residual gas pressure in Torr, and r_{e} and r_{p} are the classical electron and proton radii, respectively. A is the atomic mass number, and L_{sep} is the bunch spacing. Because the average beam current is 1 A in our design, the charge of a single bunch is thus 2 nC for a fundamental RF of 500 MHz, and all the RF buckets are filled at a harmonic number of 61. CO is chosen as the residual gas in our calculation because its ionization cross section is 6 times that of H_2, and the gas pressure is set to 10^{-9} Torr, which is not hard to reach in storage rings [26, 27]. In addition to the parameters in Table 1, we have a rising time of 0.63 ms for the instability, which is within the bandwidth of the feedback system [27]. Therefore, we conclude that the FII in our machine can be well-controlled with a relatively high but achievable vacuum level.

Furthermore, intrabeam scattering and Touschek scattering are also important collective effects in high-current storage rings. As mentioned in the preceding section, the growth rates of both scattering effects are inversely proportional to the transverse emittance of the beam. Because the nominal transverse emittance in our design is one order larger than that of third-generation light sources (or even larger), the above two effects can also be controlled.

As in other storage rings, the collective instabilities in our machine can be addressed by both chromaticity shifting and transverse feedback. However, as above-mentioned, because shifting the chromaticity to a positive value may also excite some higher-order modes of the head-tail instability, it alone is not sufficient for good control of the instabilities. Therefore, as in SOLEIL, transverse bunch-by-bunch feedback will be combined with chromaticity [28] to relieve the collective instabilities in our machine.

Finally, we must point out again that we use copper as the beam pipe material, and the inner radius of the vacuum chamber is 25 mm. According to the first-order geometric strength K_1 of the quadrupoles and the second-order strength K_2 of the sextupoles, the maximum integrated field for the strongest quadrupole is 1.36 T/m, and the maximum integrated field for the strongest sextupole is 163.3 T/m^2, which are not hard to achieve for the 400 MeV electron beam in the vacuum pipe as described above. Moreover, more detailed work is needed to provide more precise estimations of the collective effects in our design, such as the coupled-bunch instability and beam loading. These effects are topics for further investigation.

In conclusion, we believe that most of the typical collective instabilities that may arise in our machine can be controlled using feasible methods. However, as mentioned in Sect. 1, the emittance of our ring is not of great importance; therefore, the tolerance of the collective instabilities of our machine could be slightly larger than those of other storage ring light sources, which can be considered to give our design an advantage over others.

3 Considerations regarding EUV radiation

The typical wavelength currently used for EUVL is 13.5 nm. As in other machines, an undulator is employed to provide the required radiation. To evaluate the performance of our design, the SPECTRA simulation code [29–31] was used. In the simulation, a photon beam with an emittance of 40 nm in the horizontal direction and 4 nm in the vertical direction is obtained by the convolution of the electron beam and diffraction phase spaces. Strong magnets are required to obtain a maximum field exceeding 0.3 T with a period length of 15 mm. The simulation result shows that the undulator parameter is approximately 0.47. To obtain the highest photon flux, the entire central cone of the photon emission must be focused on the sample, for example, a microchip.

The parameters of the undulator as calculated by SPECTRA are shown in Table 2. According to the design parameters of the storage ring, the required 13.5 nm EUV radiation can be obtained using the undulator. According to the data in Table 2, we can see that for an average current of 1 A and a 7 m undulator, the total radiation power within 5% bandwidth (FWHM) at 13.5 nm is 4.1 W and can also exceed 10 W with a > 2 A beam current. Note, however, that in these cases, the undulator gap is approximately 10 mm, and the wakefield induced by the undulator will be somewhat strong. A superconducting undulator [32] may be required to avoid this possibility, and the overall cost may rise. Alternatively, an economical method is to lower the average beam current to several hundred milliamps to reduce the wakefield dramatically and afford much easier control. Although there would be a corresponding reduction in the radiation power to a few watts, we can still use the machine for mask inspection, as at the COSAMI. On the other hand, because the radiation power is proportional to the undulator length, the required radiation power can also be obtained by decreasing the beam current and increasing the undulator length, which is easier to realize than a higher beam current in the real machine without excessive cost. Moreover, a long variable-gap undulator can be made by combining several short sections with a dedicated control and a diagnostic system, whereas there is no such problem for the fixed gap undulator.

Furthermore, in our design, the bunch charge, duty factor of the RF bucket, and undulator gap can all be varied. Therefore, a wide radiation power range can be obtained to expand the use of our design under different conditions and at different costs. This characterizes our design as a versatile tool for various EUVL applications.

4 Conclusion

A systematic physical design study of a compact 400 MeV storage-ring-based EUV light source for industrial lithography was conducted. Owing to its compactness, reduced complexity, and relatively low cost, the storage ring can provide an average beam current of up to 1 A with a dynamic aperture of approximately $\pm$ 10 mm. If the third harmonic cavity is used, an average Touschek lifetime of 1.3 h can also be achieved. Moreover, the collective effects were also estimated at high average current. It was found that the typical collective instabilities can be controlled and relieved by implementing appropriate materials and methods, such as a copper beam pipe and modern feedback technology. With the designed undulator, the machine can radiate at 13.5 nm in the EUV regime with an average radiation power within the bandwidth of several watts to more than 10 W. Although the radiation power in the bandwidth appears to be inadequate for direct

Table 2 Basic design parameters of undulator and key indexes of EUV light

Parameter	Value
Radiation wavelength (nm)	13.5
Average beam current (A)	1
Maximum field (T)	0.337
Undulator parameter *K*	0.472
Periodic length (mm)	15
Total length (m)	7
Total radiation power (W)	80
Radiation power within 5% bandwidth (FWHM) of 13.5 nm (W)	4.1

photolithography, our design can still be used for multiple lithographic applications, such as wafer mask inspection, EUV mirror characterization, and reflectivity measurements of EUV multilayer coatings. In conclusion, our study demonstrates the feasibility of a less complex, less costly compact-storage-ring-based EUV light source with tunable current and radiation power. As an alternative to the conventional EUVL technology, it provides a new option for multiple applications in EUVL and a valuable reference for the design of similar facilities in the future.

Acknowledgements The authors would like to thank Dr. Bo-Cheng Jiang for useful discussions on storage ring physics, Dr. Zhen Wang for assistance with SPECTRA, Dr. Chao Feng for advice on the undulator, Dr. Xiao-Xia Huang for assistance with the impedance calculation, Dr. Yi-Yong Liu for the vacuum pipe calculation, and Dr. Wei Zhang for advice on the magnets.

Author contributions All authors contributed to the study conception and design. Material preparation, data collection, and analysis were performed by Si-Qi Shen, Da-Zhang Huang, and Zhen-Tang Zhao. The first draft of the manuscript was written by Si-Qi Shen, and all authors commented on subsequent versions of the manuscript. All authors read and approved the final manuscript.

References

1. O. Wood, E.U.V. Lithography, New metrology challenges. AIP Conf. Proc. **931**, 375 (2007). https://doi.org/10.1063/1.2799401
2. A. Hassanein, T. Sizyuk, Laser produced plasma sources for nanolithography—recent integrated simulation and benchmarking. Phys. Plasmas **20**, 053105 (2013). https://doi.org/10.1063/1.4807379
3. U. Stamm, Extreme ultraviolet light sources for use in semiconductor lithography—state of the art and future development. J. Phys. D Appl. Phys. **37**(23), 3244 (2004). https://doi.org/10.1088/0022-3727/37/23/005
4. X. Deng, A. Chao, J. Feikes et al., Experimental demonstration of the mechanism of steady-state microbunching. Nature **590**, 576–579 (2021). https://doi.org/10.1038/S41586-021-03203-0
5. C. Feng, X. Deng, Review of fully coherent free-electron lasers. Nucl. Sci. Tech. **29**, 160 (2018). https://doi.org/10.1007/s41365-018-0490-1
6. C. Feng, Z. Zhao, A storage ring based free-electron laser for generating ultrashort coherent euv and x-ray radiation. Sci. Rep. **7**, 4724 (2017). https://doi.org/10.1038/s41598-017-04962-5
7. Y. Ekinci, T. Garvey, A Streun et al., A compact high-brightness accelerator-based EUV source for actinic mask inspection. in *High-Brightness Sources and Light-driven Interactions, OSA Technical Digest* (*online*) (*Optical Society of America, 2018*), *paper ET3B.5*. https://doi.org/10.1364/EUVXRAY.2018.ET3B.5
8. R. Klein, R. Thornagel, G. Ulm et al., Status of the metrology light source. J. Electron. Spectrosc. **184**, 331–334 (2011). https://doi.org/10.1016/j.elspec.2010.09.008
9. S.Y. Lee, *Accelerator Physics*, 3rd edn (World Scientific, 2013). ISBN: 978-981-4374-94-1
10. Y. Wang, M. Borland, Pelegant: a parallel accelerator simulation code for electron generation and tracking. AIP Conf. Proc. **877**, 241 (2006). https://doi.org/10.1063/1.2409141
11. J. Bengtsson, A. Streun, B. Singh et al., Control of the nonlinear dynamics for medium energy synchrotron light source, in *Proceedings of IPAC08* (2018, Vancouver), pp. 4037–4041. https://doi.org/10.18429/JACoW-IPAC2018-THPMF006
12. X. Huang, J. Corbelt, J. Safranek et al., An algorithm for online optimization of accelerators. Nucl. Instrum. Meth. A **726**, 77–83 (2013). https://doi.org/10.1016/j.nima.2013.05.046
13. A. Terebilo, Accelerator modeling with matlab accelerator toolbox, in *Proceedings of PAC01* (Chicago, 2001), pp. 3203–3205. doi: https://doi.org/10.1109/PAC.2001.988056
14. W.B. Song, L. Shang, F.L. Shang et al., Nonlinear kicker design and research for Hefei advanced light facility. Nucl. Tech. **44**(6), 060202 (2021). https://doi.org/10.11889/j.0253-3219.2021.hjs.44.060202 (in Chinese)
15. J. Tong, G. Mu, B. Liu et al., Design simulation and magnetic field measurement of eddy-current type thin septum magnet for beam injection of diffraction limited storage ring. Nucl. Tech. **43**(12), 120202 (2020). https://doi.org/10.11889/j.0253-3219.2020.hjs.43.120202 (in Chinese)
16. R. Nagaoka, K.L.F. Bane, Collective effects in a diffraction limited storage ring. J. Synchrotron Rad. **21**, 937–960 (2014). https://doi.org/10.1107/S1600577514015215
17. N. Carmignani, Touschek lifetime studies and optimization of the European synchrotron radiation facility. Ph.D. thesis, University of Pisa, Italy (2016). https://doi.org/10.1007/978-3-319-25798-3
18. P.S. Dester, F. Sa, L. Liu, Energy acceptance and on momentum aperture optimization for the Sirius project. J. Phys. Conf. Ser. **874**(1), 012068 (2017). https://doi.org/10.1088/1742-6596/874/1/012068
19. W. Wu, K. Xuan, W. Xu et al., Development of a control system for the fourth-harmonic cavity of the HLS storage ring. Nucl. Sci. Tech. **29**, 153 (2018). https://doi.org/10.1007/s41365-020-00836-0
20. K.Y. Ng, Physics of Intensity Dependent Beam Instabilities (World Scientific, 2006). ISBN: 981-256-342-3
21. A.W. Chao, K.H. Mess, M. Tigner et al., *Handbook of Accelerator Physics and Engineering*, 2nd edn. (World Scientific, Singapore, 2013). https://doi.org/10.1142/8543
22. H. Wiedemann, *Particle Accelerator Physics*, 3rd edn. (Springer, Berlin, 2015). https://doi.org/10.1007/978-3-319-18317-6
23. M.S. Zisman, ZAP User's Manual, LBL-21270 (1986). https://doi.org/10.2172/6609901
24. P. Kernel, R. Nagaoka, J.-L. Revol et al., High current single bunch transverse instability at the ESRF: a new approach, in *Proceedings of EPAC 2000* (Vienna, 2000). https://accelconf.web.cern.ch/e00/PAPERS/WEP4B04.pdf
25. T.O. Raubenheimer, F. Zimmermann, Fast beam-ion instability. I. Linear theory and simulations. Phys. Rev. E **52**, 5487 (1995). https://doi.org/10.1103/PhysRevE.52.5487
26. P.C. Liu, Q.Y. Liu, Z.J. Ma et al., Design of gas bremsstrahlung absorber at high energy photon source beamlines. Nucl. Tech. **43**(9), 090102 (2020). https://doi.org/10.11889/j.0253-3219.2020.hjs.43.090102(inChinese)
27. K. Ohmi, Numerical study for the two-beam instability due to ions in electron-storage rings. Phys. Rev. E **55**, 7550 (1997). https://doi.org/10.1103/PhysRevE.55.7550
28. R. Nagaoka, L. Cassinari, J.-C. Denard et al., Transverse feedback development at SOLEIL, in *Proceedings of PAC07* (Albuquerque, 2007). https://doi.org/10.1109/PAC.2007.4440145
29. T. Tanaka, Numerical methods for characterization of synchrotron radiation based on the Wigner function method. Phys. Rev. ST Accel. Beams **17**, 060702 (2014). https://doi.org/10.1103/PhysRevSTAB.17.060702
30. T. Tanaka, Coherent mode decomposition using mixed Wigner functions of Hermite-Gaussian beams. Opt. Lett. **42**, 1576–1579 (2017). https://doi.org/10.1364/OL.42.001576

31. T. Tanaka, Universal representation of undulator phase errors. Phys. Rev. Accel. Beams **21**, 110704 (2018). https://doi.org/10.1103/PhysRevAccelBeams.21.110704
32. S. Casalbuoni, N. Glamann, A. Grau et al., Superconducting undulators: from development towards a commercial product. Synchrotron Radiat. News **31**(3), 24–28 (2018). https://doi.org/10.1080/08940886.2018.1460171